New method for binder and carbon black detection at nanometer scale in carbon electrodes for lithium ion batteries

Lukas Pfaffmann [a, *], Stefan Jaiser [b], Marcus Müller [a], Philip Scharfer [b], Wilhelm Schabel [b], Werner Bauer [a], Frieder Scheiba [a], Helmut Ehrenberg [a]

[a] *Institute for Applied Materials, Karlsruhe Institute of Technology, Hermann-von-Helmholtz-Platz 1, D-76344, Eggenstein-Leopoldshafen, Germany*
[b] *Institute of Thermal Process Engineering – Thin Film Technology, Karlsruhe Institute of Technology, Kaiserstraße 12, D-76131, Karlsruhe, Germany*

GRAPHICAL ABSTRACT

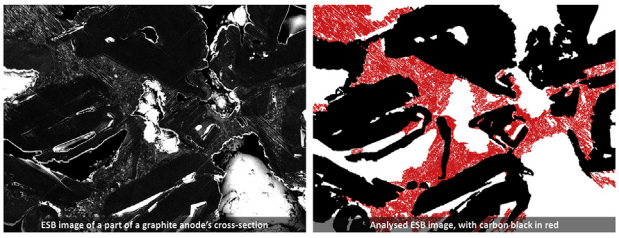

ABSTRACT

In the current work, graphite electrodes comprising PVDF binder and carbon black are subjected to characterization. An energy selective backscatter detector is used to localize carbon black and fluorine of PVDF. Therefore, it is necessary to distinguish between graphite, amorphous carbon and fluorine rich regions. Typically, an angular selective backscatter detector is employed to obtain an image providing the material contrast of the sample. Suitable materials for that detector are e.g. alloys to observe intermetallic phases, semiconductor for "channeling contrast", or imaging SiO_2 and Au nanoparticles in biological cells. However, this detector cannot be used to distinguish between light elements with low atomic numbers, such as C to P. In addition, the contrast of fluorine rich regions and graphite is poor in normal in-lens images due to the low difference of the atomic mass between C and F. The aim of this study is to enhance the contrast of fluorine rich regions to graphite to carbon black. Therefore, the energy selective backscatter detector is used and its advantages and setup is described. Finally this technique is applied to investigate 400 μm thick cross-sections of graphite electrodes dried at different temperatures and obtain the carbon black distribution.

Keywords:
Carbon electrodes
Binder
Carbon black distribution
SEM
Energy selective backscatter detector (ESB)

1. Introduction

In recent years, electric mobility evolved into an intensely discussed research topic, thereby triggering progress on many fronts. To date, lithium-ion battery technology is, however, still not fully able to compete with internal combustion engines due to limitations in volumetric energy density and costs. Research is mainly focused on identification of superior active materials. At the same

* Corresponding author. Karlsruhe Institute of Technology (KIT), Institute for Applied Materials - Energy Storage Systems (IAM-ESS), Germany.
E-mail addresses: lukas.pfaffmann@kit.edu (L. Pfaffmann), stefan.jaiser@kit.edu (S. Jaiser), marcus.mueller@kit.edu (M. Müller), philip.scharfer@kit.edu (P. Scharfer), wilhelm.schabel@kit.edu (W. Schabel), werner.bauer@kit.edu (W. Bauer), frieder.scheiba@kit.edu (F. Scheiba), Helmut.Ehrenberg@kit.edu (H. Ehrenberg).

time there is a broad acceptance in the community that manufacturing of battery cell components is equally important. Still, there is a distinct mismatch between the number of publications on materials and on manufacturing (there are only a few).

A major task during electrode processing is the adjustment of a beneficial microstructure. The microstructure and the associated electrode properties are mainly depending on the distribution of the functional additives throughout the film. In both electrodes, binder is added to provide cohesion between the particles and adhesion of the active layer to the current collector. Furthermore, incorporation of carbon black into the electrode enhances conductivity between active material particles and the current collector. Both binder and carbon black are generally considered as inactive electrode constituents as they do not contribute to the amount of stored energy but to weight and volume. Thus, their fraction should be minimized in order to maximize the volumetric energy density and to reduce costs. At the same time, binder and carbon black are decisive cell components that significantly influence the electrochemically behavior [1–8]. Minimization of functional additives requires their homogeneous distribution throughout the film along the z-coordinate. With regard to polymeric binders, there are few publications that focus on the dependency of binder distribution on the processing conditions. In this context, the drying process is of particular significance, as binder migration to the surface occurs for drying processes designed inappropriately [9–18].

However, the distribution of carbon black was not paid so much attention to as its characterization seems to be difficult. Nevertheless, the carbon black distribution is of superordinate significance for the electrodes capability of conducting electrons homogeneously. This is in particular true for oxide cathodes, where a uniform carbon black distribution gives a 50% higher capacity [19]. In literature the distribution of carbon black has only been researched into for few cathode materials ($LiMn_2O_2$-spinel, $LiCoO_2$, and $LiFePO_4$) and only by means of qualitative evaluation of SEM micrographs of electrode surfaces [20]. To our best knowledge, no publications are available that investigated into the distribution of carbon black with regard to the negative electrode. As a result, the relevant parameters that influence the carbon black distribution are still unknown. The dimensions of carbon black aggregates are, without a doubt, small enough to provide certain mobility in the porous electrode structure during drying. This assumption is reinforced by the work of several authors that succeeded in providing evidence for the accumulation of small particles at the film surface during drying [9,10,21–24]. Thus, carbon black is very likely to be capable of concentrating at the surface as well if inappropriate processing conditions are chosen. Given that, in some cases, an extremely inhomogeneous carbon black distribution could lead to clogging of surface pores, potentially implicating a weaker wetting by the electrolyte. It definitely brings about the consequence that diffusion paths of the lithium ions elongate and that the carbon black concentration decreases elsewhere in the film. Too low a concentration in the vicinity of the current collector will definitely be a threat with regard to fast charge and fast discharge processes, where the current density at the current collector increases strongly.

Jaiser et al. [14] researched binder gradients in graphite electrodes but investigated only the surface and interface regions. In another work, Jaiser et al. [15] documented the development of binder gradients throughout the film during drying by means of Cryo-BIB-SEM. Recently, Müller et al. [13] found pronounced binder gradients in graphite anodes dried at high drying rates by means of energy dispersive X-ray spectroscopy (EDS) of cross-sections prepared by broad-ion beam slope cutting (BIBSC). Due to the large reaction volume ($\approx 15\ \mu m^3$ for carbon materials [see supplemental documentation part 2]), EDS is not capable of resolving the fluorine distribution at a nanometer scale structure. Furthermore, it is not possible to separate the C-signal of the EDS-spectra to distinguish between graphite particles, binder and carbon black.

Typically, an angular selective backscatter detector is employed to obtain an image providing the material contrast of the sample. This semiconductor detector is directly mounted below the pole-piece and the electron beam strikes the target by passing through a hole in the detector [25–27]. Suitable materials for that detector are e.g. alloys to observe intermetallic phases [28], semiconductor for “channeling contrast” [29], or imaging SiO_2 and Au nanoparticles in biological cells [30]. However, this detector cannot be used to distinguish between light elements with low atomic numbers, such as C, O, F or P. At this point, the energy selective backscattered electron detection technique could provide further information. This approach is merely introduced briefly as comprehensive elaborations have been published elsewhere. More information on the basics of the in-lens and the energy selective backscattered (ESB) detector are for instance given in Refs. [26,27]. The first report on the ESB detector dates back to 2004 [31]. The ESB detector represents a second In-lens detector with a grid located in front of it, as illustrated in Fig. 1. It is positioned above the normal in-lens detector (cf. Fig. 1) [32]. Secondary electrons (SE) (green in Fig. 1) and backscattered electrons (BSE) (blue in Fig. 1) are emitted from the sample surface after excitation by an electron beam. These electrons are accelerated back into the SEM column. The electron trajectories are displayed in Fig. 1, whereas the lenses, SEM column and apertures are not drawn. The ESB grid voltage can adjusted between 0 and 1500 V to rejecting lower energy electrons [33]. Electrons of lower energy than the ESB grid are detracted before reaching the ESB detector and are not detected. By rejecting lower energy electrons (e.g. the SEs), different material compositions become distinguishable on the basis of their individual contrasts in the ESB micrographs.

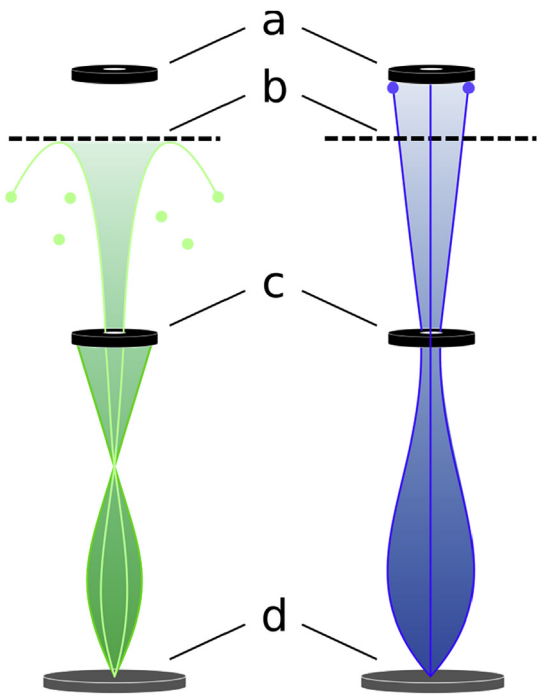

Fig. 1. Trajectories of excited electrons from the sample (d) to the in-lens detector (c) and ESB detector (a) for SE (green) and BSE (blue) electrons. The lower energy electrons (e.g. SE) cannot pass the potential which is set on the filtering grid (b). Own representation based on [38]. (For interpretation of the references to colour in this figure legend, the reader is referred to the web version of this article.)

Normally the ESB detector is used to detect the low-loss BSE electrons. That means the ESB grid voltage is only a few volts beyond the energy of the primary electrons (E_{PE}) [34,35]. This is significantly lower than the primary electron energy (10 keV or higher) generally used for conventional angular selective backscattered electron detection (ASB). As a consequence of their lower energy, electrons reaching the ESB detector will originate only from regions which are very close to the sample surface. This not only improves surface sensitivity bur also the lateral resolution due to a much smaller scattering volume when compared to ASB.

The advantage of the ESB is not only the variable grid voltage but also the so-called acceptance angle between the primary electron beam and the backscattered electrons, which is smaller in comparison to ASB detector. As a result, deeper regions (e.g. the bottom of a pore) are detectable with an ESB but not with an ASB detector, as the electrons will not be blocked by pore walls. In practice, the backscattering coefficient η (the fraction of primary electrons that escape as BSE) does increase with atomic number, but almost linearly for low atomic numbers [36]. This makes it almost impossible to obtain a suitable contrast between light elements using the ASB detector. In contrast, with the ESB detector, it is not only possible to obtain contrast between light elements, but even of different phases of the same element, e.g. graphite, diamond and amorphous carbon [37]. This knowledge can be used to identify carbon black in a graphite matrix and simultaneously detect fluorine rich regions using the ESB detector.

However, identifying the right combination of settings for the primary electron energy and the ESB grid voltage to obtain sufficient contrast between regions of different elemental composition can be a challenge. Reference samples with known local distribution as used in this work can greatly facilitate this process. Further, since the identification of different phases by ESB is based only on different yields of backscattered electrons at a certain combination of primary electron energy and ESB grid voltage, phases with very similar electron yields cannot be distinguished. This becomes especially problematic for samples consisting of several phases, since a single combination of primary electron energy and ESB grid voltage will most likely not provide optimal contrast between all phases.

Sample stability may also be an issue. Since the ESB grid rejects a large part of the electrons, the ESB signal is low. This means that high probe currents and low scan speeds need to be used to avoid high signal noise. As a consequence the sample might be damaged by the electron beam. It is therefore obligatory to verify that the sample is sufficiently stable under the chosen imaging conditions.

When compared to spectroscopic investigation methods available for electron microscopy which can provide information of the binder distribution such as EDX and wavelength-dispersive X-ray spectroscopy (WDX), the scattering volume of the ESB electrons is significantly smaller and more surface sensitive at low E_{PE}. As a result, a significantly higher lateral resolution is obtained which allows identification of much smaller sample structures.

The previous discussion evinces the need for novel approaches that allow for elucidation of the carbon black distribution. In this paper, graphite-based anodes are investigated that comprise Polyvinylidene fluoride (PVDF) as binder and carbon black as conductive agent. We image binder and carbon black at a nanometer scale by elaborating ESB technique. Smooth electrode cross-sections free of artifacts are prepared by BIBSC. By means of these methods, the carbon black distribution is revealed for 400 μm thick cross-sections by image analysis.

2. Experimental

The ESB grid voltage that has to be adjusted depends on the used E_{PE} as well as the material composition. A suitable configuration had to be figured out on a test sample first. A highly oriented pyrolytic graphite (HOPG) sample was partly coated with a thin layer of PVDF. This was done by casting PVDF on one-half of a HOPG sample and subsequent drying for 15 min at 80 °C in an oven. The other half of the HOPG sample was covered with a tape in order to prevent spreading of the PVDF solution over the pristine parts of the HOPG sample and to realize a sharp transition between the coated and the uncoated parts. The tape was carefully removed after solvent removal.

2.1. Electrode preparation

For the electrodes a commercial artificial graphite (SMG-A, Hitachi Chemicals, Japan, $d_{50} = 20$ μm) was used. By mixing the graphite with carbon black (C-NERGY C65, Imerys Graphite & Carbon, Bodio, Switzerland; BET specific surface area = 60 m^2/g), PVDF (Solef 5130, Solvay S.A., Italy) which acts as a binder, and the solvent NMP (*N*-Methylpyrrolidone) a slurry was prepared. To obtain electrode sheets the slurry was cast onto Cu foil using a continuous laboratory coater equipped with doctor-blade technology and a convection-dryer. A more detailed description of the electrode processing can be found in Refs. [14] and [13]. The interested reader is encouraged to consult the respective works for detailed information. At this point, merely the most important information is given.

Electrode samples of different microstructure, i.e. different binder and carbon black distribution, were produced to illustrate the novel approach. To provoke distinct differences, drying conditions were modified by changing the temperature a convective impingement dryer during electrode processing. Variation of drying rate was shown by several authors to result in different binder distribution and electrode properties [11,14,39]. As component gradients are pronounced for thicker films [13], electrodes that featured a thickness of 400 μm were produced through knife-coating. The low drying rate sample (LDR) was dried at 73 °C, whereas the high drying rate sample (HDR) was dried at 93 °C. A more detailed consideration of the corresponding drying parameters is given in Refs. [14,39].

2.2. Sample preparation

Two different sample preparation techniques were used, with the first as a standard. Here a small sample of 5 × 5 mm was cut with a knife from the electrodes. BIBSC was employed to produce cross-section with smooth surfaces that are free of artifacts [40]. The sample was held between two thin glass wavers during Ar-sputtering to provide a smooth edge in contrast to the rough electrode surface. The cutting is done under vacuum ($2*10^{-4}$ mbar Argon atmosphere) in an EM TIC3X triple ion beam cutter (Leica Mikrosysteme GmbH, Germany) at 7 kV and a gun current of 2.6 nA. The cutting process took around 20 h.

The second technique was used because the pores of the electrode interfere with the analysis and evaluation. Therefore silicone rubber was found to be suitable to provide the necessary contrast between carbon black and porosity for cathode materials [41,42]. The electrode was vacuum infiltrated with a silicone rubber (Wacker, ELASTOSIL RT 601). This silicone rubber provides a good viscosity (3500 mPas) and drying duration (24 h @23 °C), that all the pores are possible to fill. After the sample was dried, BIBSC is also done. The duration for one cross-section is increased to 24 h.

2.3. SEM analysis of electrode cross-section

The cross-sections were analyzed with an SEM (ZEISS-Merlin)

using both in-lens and ESB detector concurrently in dual channel mode. Images with a resolution of 4 k (4096 px times 3072 px) were stored at a magnification of 1000×, this resulted in images of 115 μm × 85 μm. To picture the entire film height of 400 μm, five images per column were compiled. The orientation of each cross-section is: top surface side and bottom collector side. Primary electron energy (E_{PE}) and ESB grid voltage were adjusted according to the results obtained from evaluation of partly coated HOPG samples (c.f. 3.1). Simultaneous to ESB detection, an in-lens image was taken of the same region. The ESB images were analyzed by image processing with 'GNU image manipulation program' (GIMP) v. 2.8 and MATLAB® v. R2016b.

3. Results and discussion

3.1. Imaging PVDF using the ESB-detector

To determine a suitable set of experimental parameters for the ESB detector with regard to the imaging of PVDF, a sample of HOPG coated one half with PVDF was analyzed by varying the ESB detector grid voltage while keeping E_{PE} fixed at 1,5 keV and 2 nA. More information, why E_{PE} is kept constant, is given in the supplementary part one.

Fig. 2 reveals a sequence of ESB images with the graphite region on the right and the PVDF coating on the left side. The actual ESB grid voltage is displayed in the top right corner. By comparing the images of Fig. 2, it is obvious that the contrast between the two regions is extremely low in the low loss mode (1480 V and 1380 V), even if the contrast setting is at its maximum at the microscope. The contrast difference increases, if the grid voltage is reduced from 1480 to 820 V. At 820 V the PVDF coated part of the HOPG can be seen as bright area, while the uncoated part is mostly black. The contrast increase at 820 V is that strong, that the contrast of the microscope has to be reduced to avoid overdrive. If the grid voltage is reduced further (below 820 V) the electron yield (brightness) of both parts if the sample increases, but more so for the carbon region, resulting in a reduced contrast. The physical reason behind this contrast effect is the inelastic interaction of primary electrons with K-shell electrons of fluorine. The binding energy for an F K 1s electron is 696.7 eV [43,44]. After the inelastic scattering process, the total energy of the primary and the K 1s electron is $E_{PE} - 696.7$ eV, which is 803.3 eV for $E_{PE} = 1{,}5$ keV. This energy is shared by these two electrons. However, the interaction with material increases in case of lower energy electrons, which means that the mean free path of these electrons is reduced [45] and most of these electrons are absorbed by the material. Even if these two electrons leave the material without any interaction, the energy is too low to get over the ESB grid potential. This is the reason, why the brightness of the fluorine rich region increases less than the graphite region if the ESB-grid voltage is lower than 820 V. Therefore the ESB grid voltage is set to 820 V for the measurements of the cross-sections to have a maximum contrast between the graphite and PVDF.

3.2. Binder and carbon black distribution by ESB analysis

Prior to measurement of the entire cross-section, a high resolution EDS mapping, in-lens and ESB image were taken from the same region to verify that the EDS detection of fluorine rich regions corresponds to fluorine rich regions in the ESB image (Fig. 3): Both EDS mapping and ESB show that some regions between the graphite particles contain more fluoride i.e. binder. However, the ESB image offers a significantly better resolution of details. The cross-sections of the graphite particles appear dark in the ESB image as expected (Fig. 3b), while the surfaces of the graphite

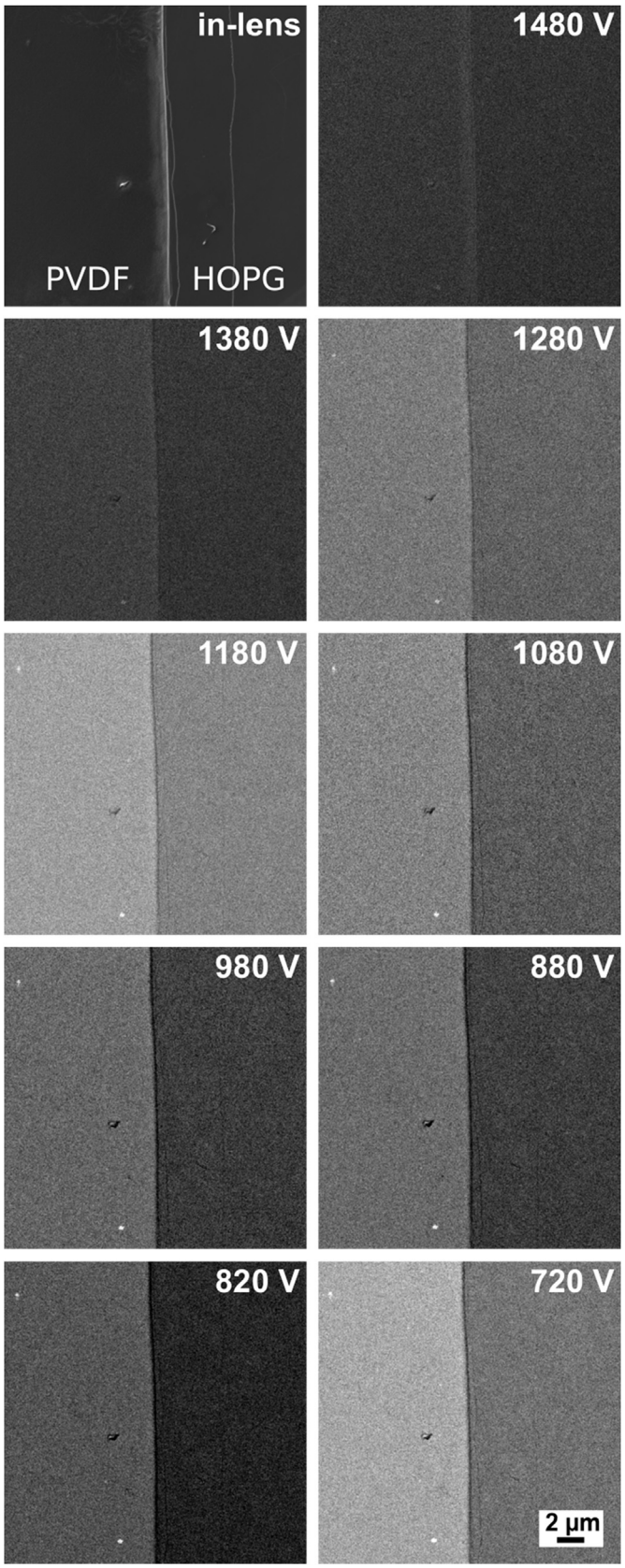

Fig. 2. Imaging a thin PVDF layer on a HOPG sample with the in-lens detector (first image) and ESB detector at different ESB-Grid voltages (upper corner). The PVDF layer is on the left side.

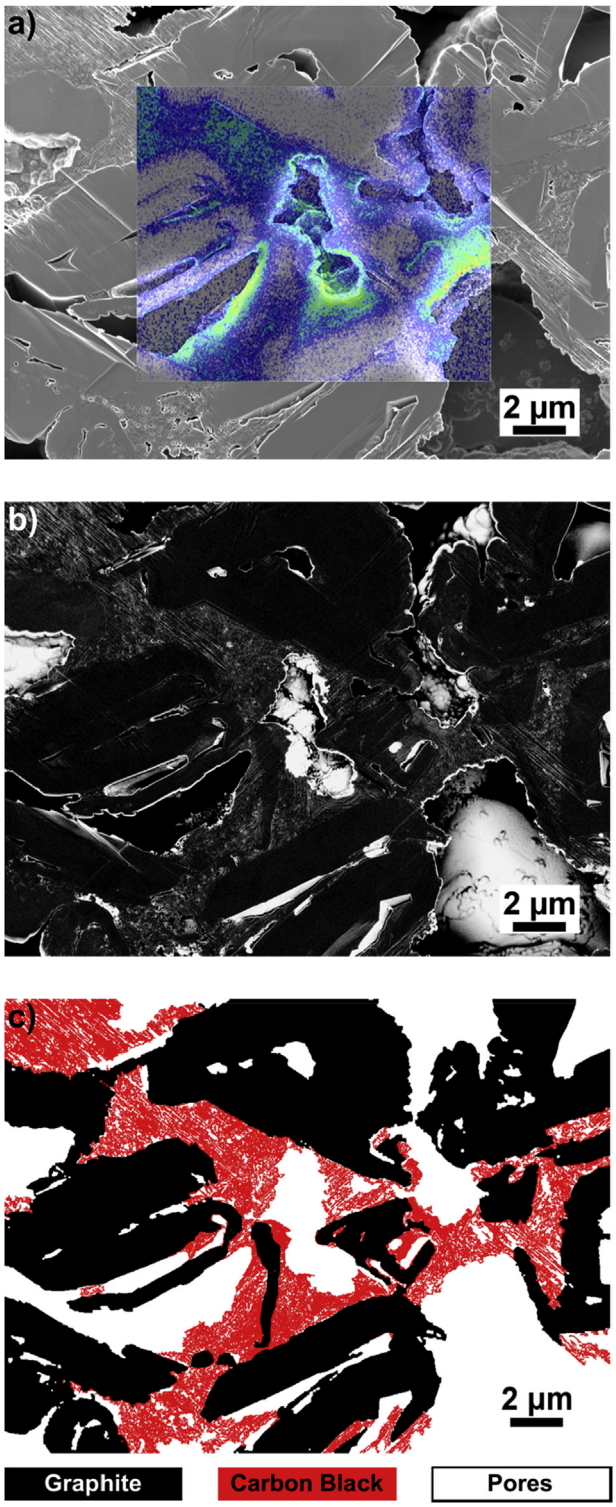

Fig. 3. High resolution area of the HDR sample. a) In-lens-image with the EDX-map; b) The ESB-image at 1.5 keV E_{PE} and 820 V on the ESB-Grid; c) Analyzed ESB-image with graphite particles in black, carbon black in red and pores in white. (For interpretation of the references to colour in this figure legend, the reader is referred to the web version of this article.)

particles (seen in some pores and at the edges) appear very bright, suggesting that they are entirely coated with PVDF. However, other effects may contribute to the brightness increase at particle surfaces and edges:

1. Edge effect
2. Material re-deposition
3. Fluorine rich regions.

To understand the first effect, it is necessary to know that the ESB detector is built of an in-lens detector. For the in-lens detector it is known that edges of the sample of the surface appear brighter [46,47], due to the acceptance angle, resulting in a more surface-sensitive image. This can also be seen in some parts of the in-lens images (c.f. 3a, 4a, 5a) but not as intense. Material re-deposition always occurs during BIBSC. The material sputtered during ion-polishing can redeposit to some part in pores of the sample. Normally, the re-depositioned material has a lower density. As a result, the BSE yield should be lower. However, a thin glass plate was placed in front of the anode to provide a smooth edge for improving the polishing result. Therefore, silicon re-deposition may occur. EDS measurements showed no proof for silicon re-deposition, but may just not be sensitive enough. If silicon is present its amount is low and therefore only forms a thin layer on the surface. ESB detection is much more sensitive to small compound variations than EDS detection, especially in near surface regions. Thus, a small silicon amount may produce higher brightness in the images, which must be taken into account for image interpretation. However, the effect should be more intense for pores located near the glass wafer (top part in the image of the cross-sections), but no change in brightness for pores near the surface (closer to the glass waver) compared to pores near the interface (far away to the glass waver) could be observed. The two described effects can therefore not fully account for the observed increased brightness of edges and pores and hence must reflect fluorine rich regions. Comparing the pores and edges of an entire cross-section (Fig. 5), one can conclude that all graphite particles are covered/coated with a thin PVDF layer.

Between the graphite particles light grey regions can be observed. At higher magnification it can be seen that these regions are not homogeneously grey and that they consist of carbon black particles. In the EDX map, the carbon black regions contain more fluorine than the surfaces of the graphite particles. This means, that the small carbon black particles are also covered with PVDF. The reason for the virtually higher concentration is that EDS averages the concentration over a rather large interaction volume (about 15 cubic µm). The interaction volume involves more fluorine in agglomerations of carbon black compared to the interaction volume at a coated graphite particle surface. In consequence, carbon black appears brighter in ESB images compared to the surface of graphite particles.

After the interpretation of contrast for cross-sections is verified, the images can be analyzed. Therefore, the images are loaded into an image processing program (GIMP v. 2.8) and manually marked with colors: cross-sections of the graphite are marked black, the carbon black regions are marked red and the pores in white. The manual marking is necessary because the grey level information e.g. of the graphite is not uniform and overlaps with other parts of the image. Additionally, deep pores of the electrode and small pores in the carbon black appear black, too. The analyzed ESB image of Fig. 3b is in Fig. 3c. This process makes the analysis and interpretation of the ESB images very time-intensive. Furthermore, the manually marking is very error-prone. The greatest difficulties in the evaluation are the pores of the anode. A solution to this problem would be to fill the pores with a material with sufficient contrast to distinguish it from the other electrode components. This material should possess a good electron conductivity to avoid charging during SEM measurements and a low viscosity for infiltration in order to fill even small pores. ELASTOSIL RT 601 (Wacker), a silicone rubber also used as encapsulation material for electronics, almost ideally matches these requirements and was therefore chosen as an

infiltration material.

Beyond the eased identification of pores, infiltration has other benefits. Since the silicon rubber also infiltrates the small pores between the carbon black particles, the carbon black structure will be stabilized for sectioning by BIBSC and the disintegration of carbon black particle is avoided. The biggest improvement is that the ESB images can now be automatically evaluated. For this purpose, a MATLAB® program was written. The manual evaluation is compared to the automated in supplementary part 3, demonstrating that the results of automated MATLAB® evaluation are comparable with the manual masking. The automated evaluation can even be considered more accurate because even small structures are masked, which is not possible in manual masking. However, there is also a disadvantage of the infiltration. Due to the high contrast of the infiltration material also in ESB it is no longer possible to analyze the thin PVDF structures on the surface of graphite and carbon black particles.

The infiltrated samples were polished by BIBSC and measured by ESB using the same settings as before. In the ESB images of the infiltrated samples the silicone rubber appears very bright (Fig. 4). Even small pores between carbon black particles are infiltrated as desired (Fig. 4d). In this electron micrograph a major advantage of the ESB detector becomes apparent: much of finer structures can be resolved compared to regular ASB images. The graphite cross-sections as well as carbon black regions have about the same brightness as the non-infiltrated samples. In the top part of the images, i.e. closer to the surface of the anode, the amount of carbon black is higher Fig. 4a. At higher resolution it can be seen, that small pores (black in ESB image) exists between the carbon black particles, which are not infiltrated. These pores are most likely not filled with silicone rubber, because their pore space is secluded, i.e. these pores are not accessible to the resin and therefore also not to the electrolyte. This may be, because the carbon black agglomerates are either very densely packed in these regions, so that pore openings can be locked by PVDF binder or that they contain an increased amount of binder locking of even larger pore openings. An indication for the latter is that the porous parts in the carbon black are surrounded by non-porous parts appearing in a slightly lighter grey, e.g. in the lower right corner of Fig. 4b. Secluded pores can also be seen in some graphite particles. The effect may therefore be used to determine the internal (closed) porosity of the electrode or the graphite particles. In the region closer to the current collector (bottom part of the image), the carbon black agglomerations have open pore space and are therefore surrounded by silicone rubber (Fig. 4c). From these results it can be concluded, that carbon black as well as PVDF binder is moving towards the top of the electrode layer. The binder seems to be contained mostly in the carbon black regions and the high amount of binder in these regions leads to a locking of pores.

3.3. *Quantification of the carbon black and binder distribution of LDR and HDR samples*

In order to study the effect of the drying rate on the carbon black and pore distribution images of electrode cross-sections covering the whole electrode thickness were either manually (non-infiltrated sample) or automatically (infiltrated sample) masked in graphite, carbon black and pore areas as described previously for

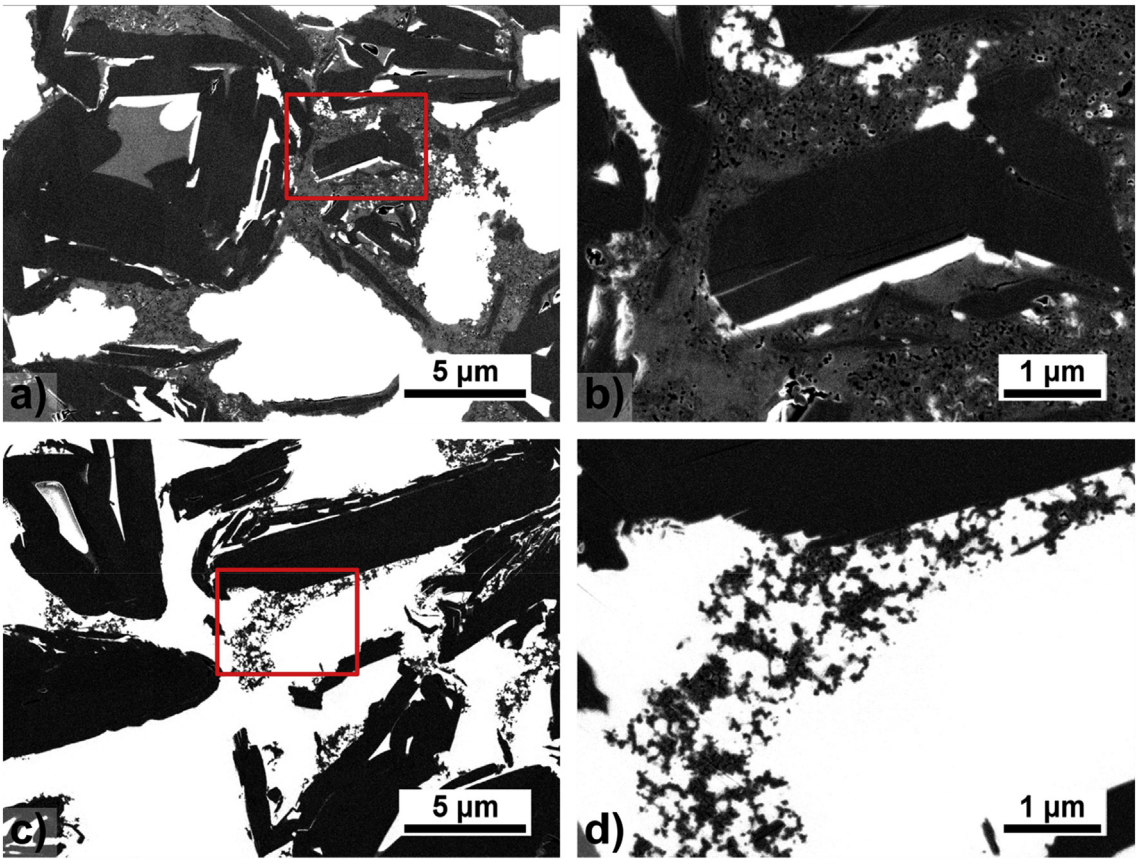

Fig. 4. ESB images of the anode filled with silicone rubber. a) region near the surface. b) higher magnification of the red area in a. c) Region in the lower third. d) higher magnification of the red area in c. (For interpretation of the references to colour in this figure legend, the reader is referred to the web version of this article.)

Fig. 3c. For quantification a set of images of a 110 μm wide part of the LDR and HDR sample were measured. The in-lens and ESB images of each sample were merged to one high resolution image of about 4060 × 12,000 px for the HDR sample (Figs. 5 and 7a-d) and about 4060 × 14,000 px for the LDR sample (Figs. 6 and 7e-h). The full resolution images are provided in the supplemental data. The masked ESB images are displayed in Figs. 5c, 6c and 7c,d,g + h. For quantification, the masked images were divided into horizontal slices of 33.5 μm in height corresponding to 1200 pixel. For each of the slices the relative subareas of graphite and pores were calculated by counting their pixel area by MATLAB®. The pixel area attributed to the carbon black was calculated as well. However, carbon black particles can only be found in the pore space between graphite particles, which can vary significantly from slice to slice due to the large particles sizes of the graphite compared to the slice area. Therefore, the pixel area of carbon black was not related to the total slice area but to the pore area of each slice to compensate for the effect of different porosities. The relative average amount of carbon black (from surface to interface) per slice/subarea is displayed for the non-infiltrated samples in Fig. 8a and the infiltrated samples in Fig. 8b. It can be seen that the distribution of carbon black varies for different drying conditions. A higher amount of carbon black can be found near the electrode surface (subarea 1−3) compared to the center and current collector side of the electrode. The effect is more pronounced for the HDR sample and is reproduced by the non-infiltrated (manual evaluation) and infiltrated (automatic evaluation). Differences between the two evaluation techniques must be attributed to statistical variations between the infiltrated and non-infiltrated sample as well as a more accurate calculation of the carbon black for the infiltrated sample, because the improved contrast and automated evaluation makes it possible analyze finer details. Further, the almost flat surface of the infiltrated cross-section reduces the error of counting carbon black, which is not exactly in the cutting plane of the cross-section.

Below we try to give an explanation why, especially at high drying rates, carbon black is accumulating in the upper parts of the electrode layers. At the beginning of the drying process the whole coating layer is still floating in electrolyte. At first, the solvent can only evaporate from the film surface. At a high drying rate, the loss of solvent from the surface layer cannot be compensated by back diffusion of solvent from lower parts and the top most layers may solidify while the mobility of carbon black and binder is maintained in parts further away from the surface. In that state, carbon black and dissolved binder from these parts can be transported by convection and capillary forces to upper already dried parts of the electrode. Since the current collector side is very far from the surface it is more likely that carbon black and binder migration originates from the central parts of the electrode layer. This may explain that the lowest carbon black concentration is observed around subarea 5. As the drying speed reduces from top to bottom of the electrode due to the increased diffusion length and partial pressure of the solvent, the distribution of carbon black and binder becomes more homogeneous. At a lower drying rate, the loss of solvent is mostly compensated by back diffusion from lower parts and a more homogeneous binder and carbon black distribution is maintained until the liquid phase has reduced to an extent at which a percolating graphite structure has formed. The tortuous, sieve-like structure of the graphite network will impede long range mass transport of carbon black at this point. As the loss of solvent continues, pores will open in the drying electrode structure. Due to capillary forces, large pores will open first, further reducing the mobility of carbon black and binder. However, since the smallest pores are those between the carbon black particles, binder which is still dissolved in the remaining solvent can accumulate inside carbon black rich regions.

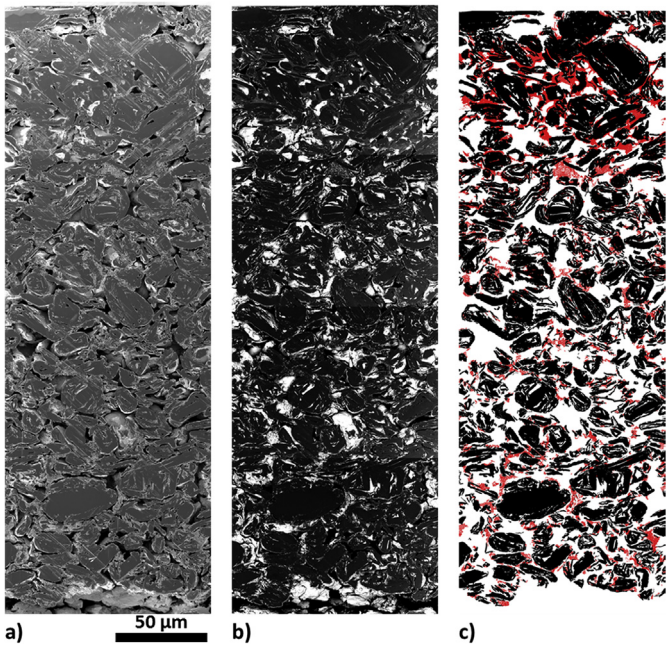

Fig. 5. HDR sample. a) in-lens image, b) ESB image, c) analyzed image. The total electrode thick-ness of this section is 334 μm.

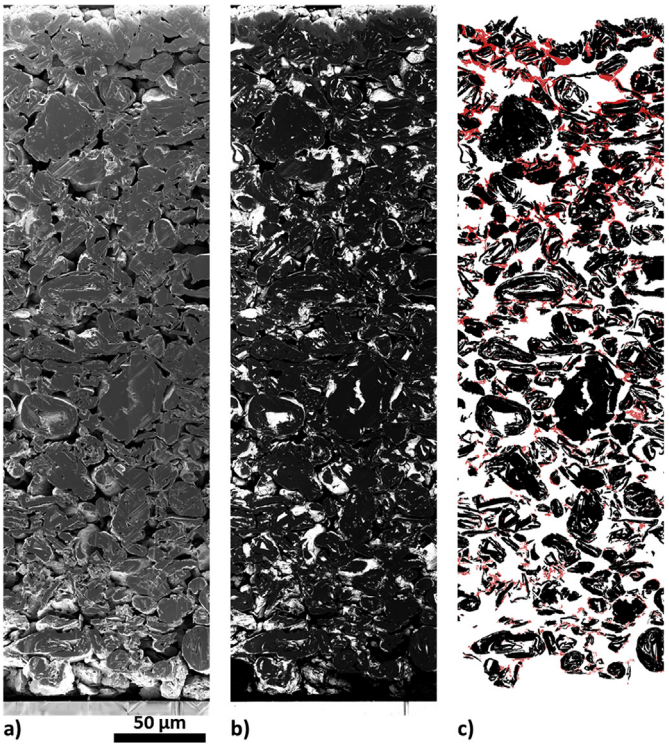

Fig. 6. LDR sample. a) in-lens image, b) ESB image, c) analyzed image. The total electrode thickness of this section is 390 μm.

4. Conclusion

ESB detection was applied to the characterization of graphite-based lithium ion battery anodes. For the first time, the drying related dependency of the distribution of carbon black throughout

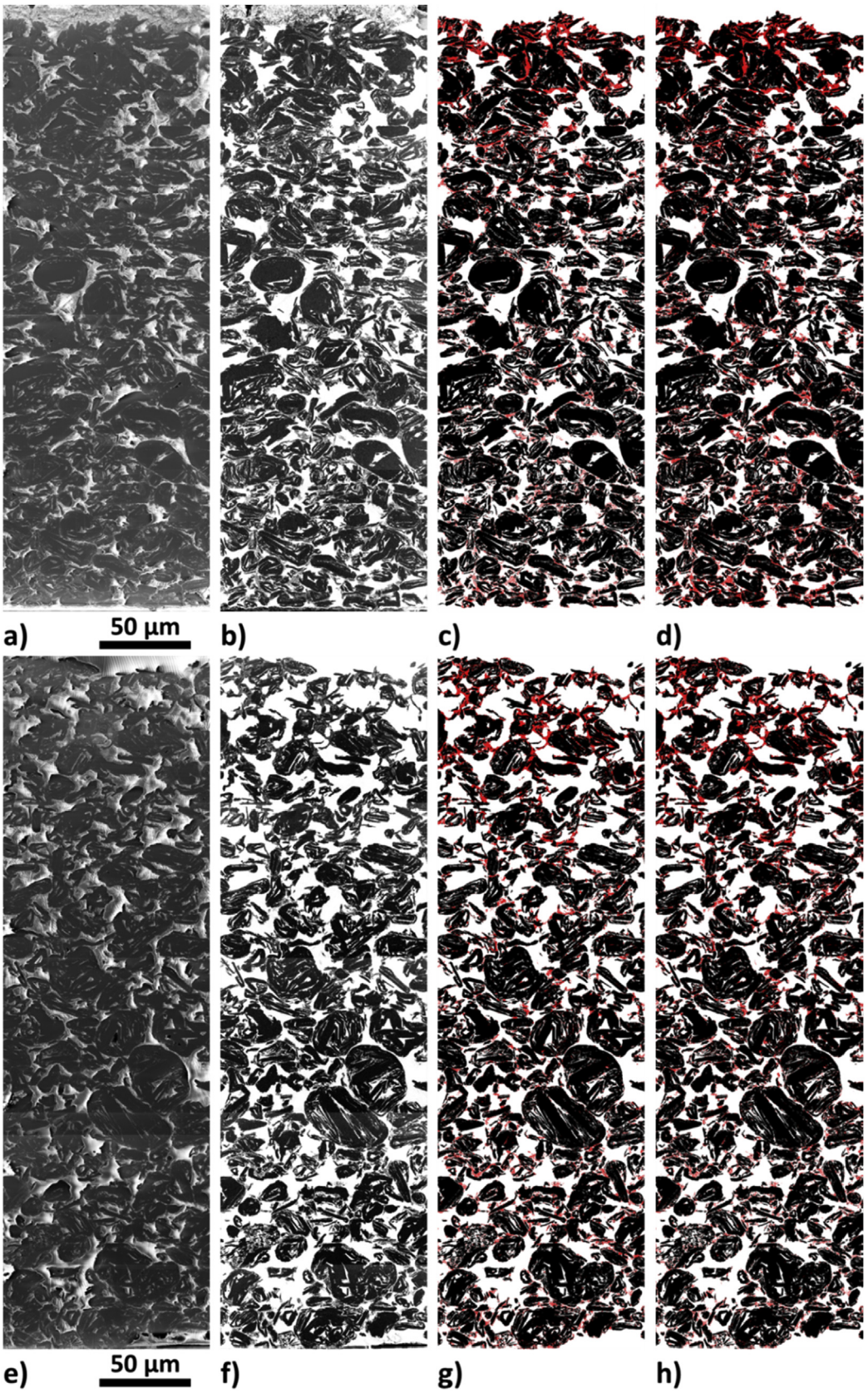

Fig. 7. HDR sample. a) in-lens image, b) ESB image, c) manually analyzed image, d) analyzed image calculated with MATLAB®. The total electrode thickness of this section is about 330 µm. And the LDR sample. e) in-lens image, f) ESB image, g) manually analyzed image, h) analyzed image calculated with MATLAB®. The total electrode thickness of the section is about 385 µm.

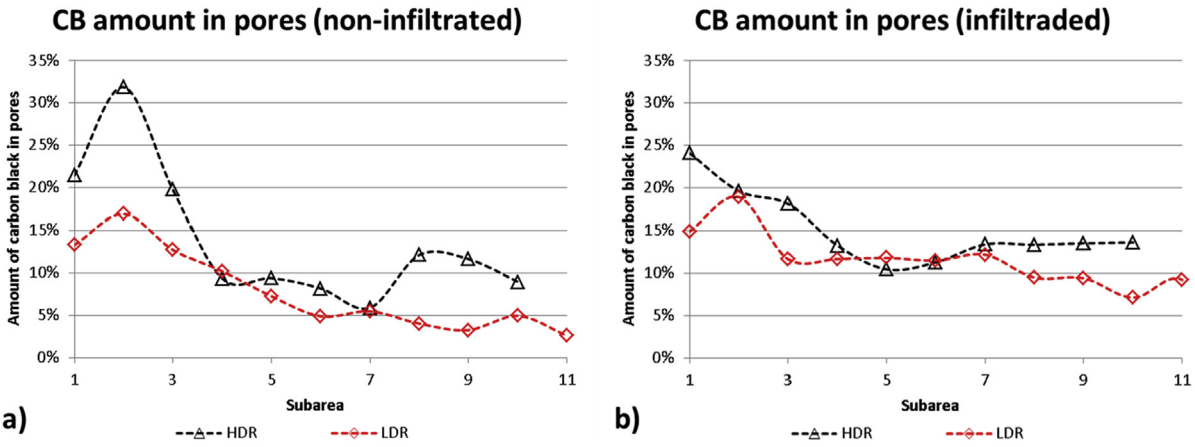

Fig. 8. Comparison of the HDR and LDR sample and its carbon black (CB) distribution in pores of the non-infiltrated samples (a) and the infiltrated (b) samples, which is calculated with MATLAB®.

the electrode was investigated. ESB grid voltage and the primary electron energy (E_{PE}) were optimized in order to allow for differentiation between the graphite active material particles on the one hand and carbon black and PVDF on the other. This was, so far, not feasible by means of ASB detection of backscattered electrons for lighter elements.

On 400 μm thick electrodes, dried at different temperatures, it was demonstrated that the binder and the carbon black can be localized at cross-sections, whereby the ESB detection is sensitive to fluorine detection. We could show that graphite particles and carbon black are covered with fluorine, independent on the drying temperature. As the fluorine concentration is higher at carbon black rich film domains, the carbon black appears brighter in the ESB images. This effect is used to evaluate the carbon black distribution by analyzing the ESB images. The evaluation of the ESB images is not that accurate for cross-sections with pores. Therefore the samples were filled with a silicone rubber. This improves the ESB images, so that it is possible to evaluate the images by MATLAB®. The result of the measurement shows that the distribution of the carbon black is not homogeneous over the cross-section and differs a lot for different drying temperatures. The amount of carbon black is higher at the surface region and decreases linearly for the low drying rate sample from surface to the middle of the cross-section. Furthermore it can be determined that the carbon black distribution correlates with fluorine distribution measured by EDS in Ref. [13].

Now this technique is going to be transferred to cathode electrodes. However, due to the presence of heavier elements (for example NMC: nickel, manganese, cobalt) in the cathode, which will produce more backscattered electrons compared to fluorine, the ESB grid voltage and the primary electron energy have to be adjusted and the infiltration material might has to be changed.

Acknowledgements

The ZEISS MERLIN SEM was financially supported by the Federal Ministry of Economics and Technology on the basis of a decision by the German Bundestag within the BMBF grant no. 03ET6017. We kindly thank Hitachi for the artificial graphite support.

References

[1] C.-C. Li, Y.-W. Wang, Binder distributions in water-based and organic-based LiCoO2 electrode sheets and their effects on cell performance, J. Electrochem. Soc. 158 (2011) A1361, http://dx.doi.org/10.1149/2.107112jes.
[2] J. Chen, J. Liu, Y. Qi, T. Sun, X. Li, Unveiling the roles of binder in the mechanical integrity of electrodes for lithium-ion batteries, J. Electrochem. Soc. 160 (2013) A1502–A1509, http://dx.doi.org/10.1149/2.088309jes.
[3] G. Liu, H. Zheng, X. Song, V.S. Battaglia, Particles and polymer binder interaction: a controlling factor in lithium-ion electrode performance, J. Electrochem. Soc. 159 (2012) A214, http://dx.doi.org/10.1149/2.024203jes.
[4] S. Chou, Y. Pan, J. Wang, H. Liu, S. Dou, Small things make a big difference: binder effects on the performance of Li and Na batteries, Phys. Chem. Chem. Phys. 16 (2014) 20347–20359, http://dx.doi.org/10.1039/c4cp02475c.
[5] Z. Zhang, T. Zeng, Y. Lai, M. Jia, J. Li, A comparative study of different binders and their effects on electrochemical properties of LiMn2O4 cathode in lithium ion batteries, J. Power Sources 247 (2014) 1–8, http://dx.doi.org/10.1016/j.jpowsour.2013.08.051.
[6] B. Lestriez, Functions of polymers in composite electrodes of lithium ion batteries, Compt. Rendus Chim. 13 (2010) 1341–1350, http://dx.doi.org/10.1016/j.crci.2010.01.018.
[7] L. Fransson, T. Eriksson, K. Edstr??m, T. Gustafsson, J.O. Thomas, Influence of carbon black and binder on Li-ion batteries, J. Power Sources 101 (2001) 1–9, http://dx.doi.org/10.1016/S0378-7753(01)00481-5.
[8] H.C. Shin, W. Il Cho, H. Jang, Electrochemical properties of carbon-coated LiFePO4 cathode using graphite, carbon black, and acetylene black, Electrochim. Acta 52 (2006) 1472–1476, http://dx.doi.org/10.1016/j.electacta.2006.01.078.
[9] S. Lim, K.H. Ahn, M. Yamamura, Latex migration in battery slurries during drying, Langmuir 29 (2013) 8233–8244, http://dx.doi.org/10.1021/la4013685.
[10] H. Hagiwara, W.J. Suszynski, L.F. Francis, A Raman spectroscopic method to find binder distribution in electrodes during drying, J. Coatings Technol. Res. 11 (2014) 11–17, http://dx.doi.org/10.1007/s11998-013-9509-z.
[11] B.G. Westphal, H. Bockholt, T. Günther, W. Haselrieder, A. Kwade, Influence of convective drying parameters on electrode performance and physical electrode properties, ECS Trans. 64 (2015) 57–68, http://dx.doi.org/10.1149/06422.0057ecst.
[12] T. Günther, N. Billot, J. Schuster, J. Schnell, F.B. Spingler, H.A. Gasteiger, The manufacturing of electrodes: key process for the future success of lithium-ion batteries, Adv. Mater. Res. 1140 (2016) 304–311, http://dx.doi.org/10.4028/www.scientific.net/AMR.1140.304.
[13] M. Müller, L. Pfaffmann, S. Jaiser, M. Baunach, V. Trouillet, F. Scheiba, et al., Investigation of binder distribution in graphite anodes for lithium-ion batteries, J. Power Sources 340 (2017) 1–5, http://dx.doi.org/10.1016/j.jpowsour.2016.11.051.
[14] S. Jaiser, M. Müller, M. Baunach, W. Bauer, P. Scharfer, W. Schabel, Investigation of fi lm solidi fi cation and binder migration during drying of Li-Ion battery anodes, J. Power Sources 318 (2016) 210–219, http://dx.doi.org/10.1016/j.jpowsour.2016.04.018.
[15] S. Jaiser, J. Kumberg, J. Klaver, J.L. Urai, W. Schabel, J. Schmatz, et al., Microstructure formation of lithium-ion battery electrodes during drying e an ex-situ study using cryogenic broad ion beam slope- cutting and scanning electron microscopy (Cryo-BIB-SEM), J. Power Sources 345 (2017) 97–107, http://dx.doi.org/10.1016/j.jpowsour.2017.01.117.
[16] S. Jaiser, N.S. Salach, M. Baunach, P. Scharfer, W. Schabel, The impact of drying conditions and wet film properties on adhesion and film solidification of lithium ion battery anodes, Dry. Technol. 3937 (2017), http://dx.doi.org/

10.1080/07373937.2016.1276584, 07373937.2016.1276584.
[17] S. Jaiser, A. Friske, M. Baunach, P. Scharfer, W. Schabel, Development of a three-stage drying profile based on characteristic drying stages for lithium-ion battery anodes, Dry. Technol. 3937 (2017), http://dx.doi.org/10.1080/07373937.2016.1248975, 07373937.2016.1248975.
[18] S. Jaiser, L. Funk, M. Baunach, P. Scharfer, W. Schabel, Experimental investigation into battery electrode surfaces: the distribution of liquid at the surface and the emptying of pores during drying, J. Colloid Interface Sci. 494 (2017) 22–31, http://dx.doi.org/10.1016/j.jcis.2017.01.063.
[19] R. Dominko, M. Gaberšček, J. Drofenik, M. Bele, J. Jamnik, Influence of carbon black distribution on performance of oxide cathodes for Li ion batteries, Electrochim. Acta 48 (2003) 3709–3716, http://dx.doi.org/10.1016/S0013-4686(03)00522-X.
[20] R. Dominko, M. Gaberscek, J. Drofenik, M. Bele, S. Pejovnik, J. Jamnik, The role of carbon black distribution in cathodes for Li ion batteries, J. Power Sources 119–121 (2003) 770–773, http://dx.doi.org/10.1016/S0378-7753(03)00250-7.
[21] Y. Ma, H.T. Davis, L.E. Scriven, Microstructure development in drying latex coatings, Prog. Org. Coatings 52 (2005) 46–62, http://dx.doi.org/10.1016/j.porgcoat.2004.07.023.
[22] H. Luo, C.M. Cardinal, L.E. Scriven, L.F. Francis, et al., Ceramic nanoparticle/monodisperse latex coatings, Langmuir 24 (2008) 5552–5561, http://dx.doi.org/10.1021/la800050u.
[23] Y.H. Zang, J. Du, Y. Du, Z. Wu, S. Cheng, Y. Liu, The migration of styrene butadiene latex during the drying of coating suspensions: when and how does migration of colloidal particles occur? Langmuir 26 (2010) 18331–18339, http://dx.doi.org/10.1021/la103675f.
[24] Y.F. Du, Y.H. Zang, Study of latex migration mechanism during coating consolidation, Adv. Mater. Res. 295–297 (2011) 83–87, http://dx.doi.org/10.4028/www.scientific.net/AMR.295-297.83.
[25] G.E. Lloyd, Atomic number and crystallographic contrast images with the SEM: a review of backscattered electron techniques, Mineral. Mag. 51 (1987) 3–19.
[26] J. Ackermann, Manual for the SUPRA (VP) and ULTRA Scanning Electron Microscope, ZEISS Man, 2005.
[27] L. Reimer, Scanning Electron Microscopy: Physics of Image Formation and Microanalysis, 2., comple, Springer, Berlin, 1998.
[28] J.M. Yu, N. Wanderka, G. Miehe, J. Banhart, Intermetallic phases in high purity Al-10Si-0.3Fe cast alloys with and without Sr modification studied by FIB tomography and TEM, Intermetallics 72 (2016) 53–61, http://dx.doi.org/10.1016/j.intermet.2016.02.003.
[29] M. Itakura, N. Kuwano, K. Sato, S. Tachibana, Variations in contrast of scanning electron microscope images for microstructure analysis of Si-based semiconductor materials, J. Electron Microsc. (Tokyo) 59 (2010) 165–173, http://dx.doi.org/10.1093/jmicro/dfq044.
[30] J. Seiter, E. Müller, H. Blank, H. Gehrke, D. Marko, D. Gerthsen, Backscattered electron SEM imaging of cells and determination of the information depth, J. Microsc. 254 (2014) 75–83, http://dx.doi.org/10.1111/jmi.12120.
[31] M.D.G. Steigerwald, R. Arnold, J. Bihr, V. Drexel, H. Jaksch, D. Preikszas, et al., New detection system for GEMINI, Microsc. Microanal. 10 (2004) 1372–1373, http://dx.doi.org/10.1017/S1431927604884083.
[32] M.D.G. Steigerwald, New Detection System for LEO FE-SEM - Ultra Low Voltage BSE Imaging, (n.d.).
[33] H. Jaksch, J. Vermeulen, New Developments in GEMINI ® FESEM Technology, By Carl ZEISS. (n.d.).
[34] K. Woo, H. Jaksch, Compositional contrast of uncoated fungal spores and stained section-face by low-loss backscattered electron imaging 40 (2004) 724–729, http://dx.doi.org/10.1016/j.micron.2009.05.001.
[35] T. Covered, I. Nanomaterials, Low Loss Backscattered Electron (BSE) Imaging - Principles and Advantages Using GEMINI ® Technology by Carl Zeiss, 2010, pp. 1–11.
[36] R.F. Egerton, Physical Principles of Electron Microscopy: an Introduction to TEM, SEM and AEM, second ed., Springer, 2016.
[37] H. Jaksch, Contrast mechanisms low-loss backscattered electrons in a field emission SEM, in: Mod. Dev. Appl. MICROBEAM Anal, 2011, p. 17.
[38] J.-P. Vermeulen, 12 Years Zeiss Gemini ® FESEM Technology, Imaging Microsc, 2004, pp. 34–35.
[39] M. Baunach, S. Jaiser, S. Schmelzle, H. Nirschl, P. Scharfer, W. Schabel, et al., Delamination behavior of lithium-ion battery anodes: influence of drying temperature during electrode processing, LDRT. 34 (n.d.) 462–473. doi: 10.1080/07373937.2015.1060497.
[40] G. Ji, Z. Tan, R. Shabadi, Z. Li, W. Grünewald, A. Addad, et al., ScienceDirect Triple ion beam cutting of diamond/Al composites for interface characterization, Mater. Charact. 89 (2014) 132–137, http://dx.doi.org/10.1016/j.matchar.2014.01.008.
[41] M. Ender, J. Joos, T. Carraro, E. Ivers-Tiffee, Quantitative characterization of LiFePO4 cathodes reconstructed by FIB/SEM tomography, J. Electrochem. Soc. 159 (2012) A972–A980, http://dx.doi.org/10.1149/2.033207jes.
[42] M. Ender, J. Joos, T. Carraro, E. Ivers-Tiffée, Three-dimensional reconstruction of a composite cathode for lithium-ion cells, Electrochem. Commun. 13 (2011) 166–168, http://dx.doi.org/10.1016/j.elecom.2010.12.004.
[43] Albert C. Thompson, David T. Attwood, Eric M. Gullikson, Malcolm R. Howells, Jeffrey B. Kortright, Arthur L. Robinson, James H. Underwood, X-ray Data Booklet, 2001 http://xdb.lbl.gov/xdb.pdf.
[44] M. Cardona, Photoemission in Solids: General Principles, Springer, 1978.
[45] M.P. Seah, W.A. Dench, Quantitative Electron Spectroscopy of Surfaces, 1979, pp. 46–55.
[46] Y. Homma, S. Suzuki, Y. Kobayashi, M. Nagase, D. Takagi, Mechanism of bright selective imaging of single-walled carbon nanotubes on insulators by scanning electron microscopy, Appl. Phys. Lett. 84 (2004) 1750–1752, http://dx.doi.org/10.1063/1.1667608.
[47] K. Kumagai, T. Sekiguchi, Sharing of secondary electrons by in-lens and out-lens detector in low-voltage scanning electron microscope equipped with immersion lens, Ultramicroscopy 109 (2009) 368–372, http://dx.doi.org/10.1016/j.ultramic.2009.01.005.